Ground-State Electronic Structures of Binuclear Iron(II) Sites: Experimental Protocol and a Consistent Description of Mössbauer, EPR, and Magnetization Measurements of the Bis(phenolate)-Bridged Complex $[Fe_2(salmp)_2]^{2-}$

Michael P. Hendrich,[†] Edmund P. Day,[‡] Chiou-Pirng Wang,[‡] Barry S. Synder,[§] Richard H. Holm,[§] and Eckard Münck*,[∥]

Department of Biochemistry, University of Minnesota, Minneapolis, Minnesota 55455, Department of Physics, Emory University, Atlanta, Georgia 30322, Department of Chemistry, Harvard University, Cambridge, Massachusetts 02138, and Department of Chemistry, Carnegie Mellon University, Pittsburgh, Pennsylvania 15213

Received January 21, 1994[⊕]

A class of proteins containing oxygen-bridged exchange-coupled binuclear iron sites can exist in various oxidation states, including the Fe^{2+}·Fe^{2+} form. A variety of techniques such as magnetic circular dichroism, EPR, Mössbauer spectroscopy, and magnetization measurements are generally being used to study the electronic structure of the low-lying levels of these clusters. Because Fe^{2+} sites exhibit large zero-field splittings, large quadrupole splittings, and substantial anisotropies of the magnetic hyperfine interactions, researchers are faced with solving a difficult multiparameter problem. In order to develop an experimental protocol for the study of iron–oxo proteins, we have investigated a structurally well-defined Fe^{2+}·Fe^{2+} center with EPR, Mössbauer spectroscopy, and saturation magnetization. Here we report a consistent set of exchange, fine structure, and hyperfine structure parameters for the $Fe_2O_6N_2$ coordination unit of $[Fe_2(salmp)_2]^{2-}$, where salmp is bis(salicylidenamino)-2-methylphenolate(3–). The techniques employed yield $J = -14$ cm^{-1} ($\mathcal{H}_{ex} = JS_1 \cdot S_2$) for the exchange coupling constant. The Mössbauer data indicate that the two ferrous sites are equivalent. A ligand field analysis shows that the ferrous sites experience a trigonal distortion of the octahedral coordination unit. The data obtained by the three techniques have been fitted with a spin Hamiltonian over a wide range of applied magnetic fields and temperatures.

Introduction

Efforts in many laboratories are currently directed toward the elucidation of the geometric and electronic structures of the binuclear oxygen-bridged iron clusters of proteins.[1] This class of proteins includes hemerythrin (Hr),[2] ribonucleotide reductase (RNR) B2 subunit, methane monooxygenase hydroxylase component (MMOH), purple acid phosphatase, rubrerythrin, and most recently stearoyl-ACP desaturase.[3] The binuclear sites can exist in three stable oxidation states: oxidized [Fe^{3+}·Fe^{3+}], mixed-valence [Fe^{3+}·Fe^{2+}], and fully reduced [Fe^{2+}·Fe^{2+}]. Mössbauer studies of MMOH have recently provided evidence for a catalytic intermediate at the Fe^{4+}·Fe^{4+} level.[4] The iron sites of the binuclear centers are exchange-coupled in all states. While the coupling is exclusively antiferromagnetic in the oxidized state, the clusters have been observed to be antiferromagnetically or ferromagnetically coupled in lower oxidation states. The fully reduced state is of particular interest from a biochemical standpoint, because it is this state that interacts with O_2 in Hr, RNR, MMOH, and presumably stearoyl-ACP desaturase. Thus, a characterization of the electronic structure of the fully reduced state is of great interest.

High-spin Fe^{3+} ($S = {}^5/_2$) has a half-filled 3d-shell, and thus the orbital contribution to its magnetic properties is minor. In contrast, high-spin Fe^{2+} ($S = 2$) complexes exhibit the features of large zero-field splittings, anisotropic **g**- and **A**-tensors, and often fast spin–lattice relaxation rates even at 4.2 K. In addition, Fe^{2+} complexes are susceptible to oxidation or bridge destruction, giving impurity species from ferric and mononuclear ferrous species. Consequently, measurement, analysis, and interpretation of ground-state magnetic properties of high-spin Fe^{2+} sites in proteins has proven considerably more difficult than a corresponding treatment of high-spin Fe^{3+} sites. The situation is potentially exacerbated when the two sites of a coupled binuclear unit are not equivalent.

One approach to an elucidation of the properties of bridged binuclear iron sites utilizes the species in Figure 1. The trianionic binucleating ligand salmp (**1**) affords the complexes $[Fe_2(salmp)_2]^{0,1-,2-}$ (**2**) whose chelating ligation mode is indicated. This set of compounds has several significant features: (i) three oxidation states containing Fe^{3+}·Fe^{3+}, Fe^{3+}·Fe^{2+}, and Fe^{2+}·Fe^{2+} have been stabilized; (ii) all three oxidation states have been isolated and structurally characterized and are interconverted by reversible electron transfer reactions; (iii) the irons in the three oxidation states are ferromagnetically exchange coupled; (iv) the mixed-valence complex $[Fe_2(salmp)_2]^-$ is valence-trapped below 100 K. The complexes **2** encompass the same set of oxidation states as in the proteins above; indeed, they constitute the only set of synthetic complexes that have been structurally defined in these three oxidation states. The structure of the $Fe_2O_6N_4$ coordination unit of $[Fe_2(salmp)_2]^{2-}$ (**3**) is set out in Figure 1.

† Present address: Department of Chemistry, Carnegie Mellon University.
‡ Emory University.
§ Harvard University.
∥ Carnegie Mellon University.
⊕ Abstract published in *Advance ACS Abstracts*, May 15, 1994.

(1) (a) Kurtz, D. M. *Chem. Rev.* **1990**, *90*, 585–605. (b) Que, L., Jr.; True, A. E. *Prog. Inorg. Chem.* **1900**, *38*, 97–200. (c) Vincent, J. B.; Olivier-Lilley, G. C.; Averill, B. A. *Chem. Rev.* **1990**, *90*, 1447–1467. (d) Sanders-Loehr, J. In *Iron Carriers and Iron Proteins*; Loehr, T. M., Ed.; VCH: New York, 1989; pp 375–466. (e) Stubbe, J. *Curr. Opin. Struct. Biol.* **1991**, *1*, 788–795.

(2) Abbreviations: salmp, bis(salicylidenamino)-2-methylphenolate(3–); EFG, electric field gradient; MMOH, methane monooxygenase hydroxylase component; Hr, hemerythrin; RNR, ribonucleotide reductase; EDTA, ethylenediaminetetraacetic acid. ACP, acyl carrier protein.

(3) Fox, B. G.; Shanklin, J.; Somerville, C.; Münck, E. *Proc. Natl. Acad. Sci., USA* **1993**, *90*, 2486–2490.

(4) Lee, S.-K.; Fox, B. G.; Froland, W. A.; Lipscomb, J. D.; Münck, E. *J. Am. Chem. Soc.* **1993**, *115*, 6450–6451.

(5) Snyder, B. S.; Patterson, G. S.; Abrahamson, A. J.; Holm, R. H. *J. Am. Chem. Soc.* **1989**, *111*, 5214–5223.

(6) Surerus, K. K.; Münck, E.; Snyder, B. S.; Holm, R. H. *J. Am. Chem. Soc.* **1989**, *111*, 5501–5502.

0020-1669/94/1333-2848$04.50/0

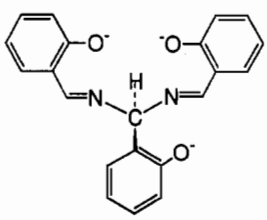

salmp (**1**)

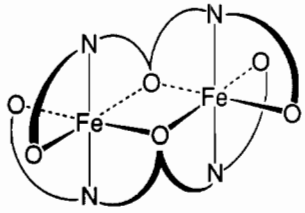

$[Fe_2(salmp)_2]^{0,1-,2-}$ (**2**)

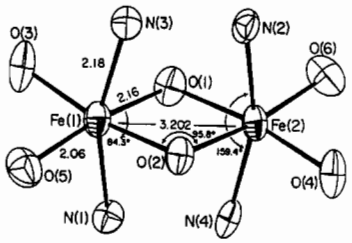

$[Fe_2(salmp)_2]^{2-}$ (**3**)

Figure 1. Trianionic binucleating ligand salmp (**1**), chelated structure of the complexes $[Fe_2(salmp)_2]^{0,1-,2-}$ (**2**), and structure of the binuclear coordination unit of $[Fe_2(salmp)_2]^{2-}$ (**3**) showing selected mean bond angles and distances.[5]

There is no crystallographically imposed symmetry; average dimensions are shown. The two Fe^{2+} atoms are bridged by phenolate oxygen atoms at a distance of 3.202 Å and exhibit distorted octahedral coordination.

Knowledge of the ground-state electronic features of coupled binuclear Fe^{2+} centers is at such a rudimentary stage that we consider an in-depth analysis of properties of a structurally well-defined species to be essential in developing a satisfactory interpretive protocol for other cases, including proteins. As will be shown, a consistent description of Mössbauer, EPR, and magnetic properties of $[Fe_2(salmp)_2]^{2-}$ can be achieved with a single set of parameters.

Materials and Methods

Preparation of Compounds. The compound $(Et_4)_2[Fe_2(salmp)_2]$ was prepared as previously described.[5] All manipulations of this air-sensitive material for physical measurements were conducted under a pure dinitrogen atmosphere. The sample concentrations are nominally 5 mM.

Mössbauer Spectroscopy. Mössbauer spectra were obtained on a constant-acceleration instrument equipped with a Janis Supervaritemp cryostat. Isomer shifts are reported relative to iron metal at room temperature. The sample temperature was carefully measured with a calibrated titanium–gallium diode (TG120, Lakeshore Cryogenics), which was positioned in the sample holder. The holder was shielded from direct helium gas flow with mylar to minimize thermal gradients. Crystallites of $(Et_4N)_2[Fe_2(salmp)_2]$ were suspended in benzene to prevent torquing of the material in an applied magnetic field.

EPR Spectroscopy. X-band EPR spectra were recorded with a Varian E9 spectrometer using an Oxford ESR-10 liquid-helium cryostat and a Varian E-236 dual mode cavity. Q-band spectra were recorded with a Varian E9 spectrometer using a cylindrical TE_{110} cavity immersed in a Cryo Industries helium cryostat. The magnetic fields of both spectrometers were calibrated with an NMR gaussmeter, and for the X-band measurements the microwave frequency was measured with a counter. For studies at variable temperatures, a 1-mm o.d. capillary tube containing $[Fe(EDTA)]^{1-}$ ($D = 0.7$ cm^{-1}, $E/D = 0.3$)[7] was imbedded into a frozen solution of $(Et_4N)_2[Fe_2(salmp)_2]$ for use as a temperature calibration standard.

Quantification of the EPR signals was accomplished with computer simulations which have normalized intensity relative to an integer spin standard.[8] The normalized intensity is adjusted for daily spectrometer variations against a $[Cu(EDTA)]^{2-}$ spin standard.

Magnetic Measurements. A concentrated solution of $(Et_4N)_2[Fe_2(salmp)_2]$ in acetonitrile was loaded into a quartz bucket for the magnetization measurements. Multifield saturation magnetization data were collected as described previously[9,10] using a Quantum Design superconducting susceptometer from 2 to 200 K at fixed fields ranging from 0.2 to 5.5 T. The saturation magnetization difference data (holder-corrected sample minus holder-corrected control) were fit using the simplex method to find the spin Hamiltonian parameter set yielding the minimum in the standard quality of the fit parameter, χ^2. The software package to carry out the data analysis is a product of WEB Research Co., Edina, MN.

Results and Analysis

Spin Hamiltonian for Analyses of Mössbauer, EPR, and Magnetization Data. The complex to be described below consists of a pair of ferromagnetically coupled high-spin ferrous ($S_1 = S_2 = 2$) ions. The two iron sites of $[Fe_2(salmp)_2]^{2-}$ are equivalent within the resolution of the Mössbauer data. Thus, it is assumed that the zero-field splitting tensors $\mathbf{D}_i$, the electronic g-tensors $\mathbf{g}_i$, the magnetic hyperfine tensors $\mathbf{a}_i$, and the EFG tensors $\mathbf{V}_i$, are the same and collinear[11] for both sites ($i = 1, 2$). The spin Hamiltonian describing the low-lying electronic states is

$$\mathcal{H}_{SS} = J\mathbf{S}_1\cdot\mathbf{S}_2 + \sum_{i=1,2}[D_i(S_{z_i}^2 - 2) + E_i(S_{x_i}^2 - S_{y_i}^2) + \beta\mathbf{S}_i\cdot\mathbf{g}_i\cdot\mathbf{H}] \quad (1)$$

where the first term describes the exchange interaction and the sum contains the zero-field and Zeeman interactions for each site. Our studies show that the first excited orbital state of the ferrous ions is at least 600 cm^{-1} above the ground state (see below). This allow us to express the x- and y-components of the $\mathbf{g}_i$-tensors using the second-order perturbation expressions,

$$g_{x_i} = g_{z_i} + 2(D_i - E_i)/\lambda \quad (2)$$

$$g_{y_i} = g_{z_i} + 2(D_i + E_i)/\lambda$$

where $\lambda = \xi/2S = -100$ cm^{-1} is the spin–orbit coupling constant.[12]

For $|J| > |D_i|$ it is useful to group the energy levels of eq 1 by multiplets of total S, where $\mathbf{S} = \mathbf{S}_1 + \mathbf{S}_2$, and to discuss the low-temperature EPR and Mössbauer data in a coupled representation.[13] In this representation, the electronic properties of the $S = 4$ multiplet can be described by

$$\mathcal{H}_c = D(S_z^2 - {}^{20}/_3) + E(S_x^2 - S_y^2) + \beta\mathbf{S}\cdot\mathbf{g}_c\cdot\mathbf{H} \quad (3)$$

where the quantities D, E, and $\mathbf{g}_c$ refer now to the coupled system. In the limit $|J| \gg |D_i|$, the parameters of eq 3 are related to those of eq 1 by the tensor relations $\mathbf{D} = ({}^3/_{14})(\mathbf{D}_1 + \mathbf{D}_2)$ and $\mathbf{g}_c = (\mathbf{g}_1 + \mathbf{g}_2)/2$.[14]

Figure 2 shows the low-lying energy levels of eq 1 as a function of $|J/D_i|$ for H = 0. For $[Fe_2(salmp)_2]^{2-}$, we will show that $|J/D_i| \approx 2$. For this ratio, the energies of the lowest nine levels are to a good approximation equal to those of an $S = 4$ multiplet. Thus, the low-temperature EPR and Mössbauer data can be analyzed using the coupled spin Hamiltonian $\mathcal{H}_c$ (eq 3) with minimal error. This simplication speeds data analysis and, in particular, allows

(7) (a) Aasa, R. *J. Chem. Phys.* **1970**, *52*, 3919–3930. (b) Lang, G.; Aasa, R.; Garbett, K.; Williams, R. J. P. *J. Chem. Phys.* **1971**, *55*, 4539–4545.
(8) Hendrich, M. P.; Debrunner, P. G. *Biophys. J.* **1989**, *56*, 489–506.
(9) Day, E. P.; Kent, T. A.; Lindahl, P. A.; Münck, E.; Orme-Johnson, W. H.; Roder, H.; Roy, A. *Biophys. J.* **1987**, *52*, 837–853.
(10) Day, E. P. *Meth. Enzymol.* **1993**, *227*, 437–463.
(11) The powder-averaged Mössbauer spectra of both iron sites are the same. This does not necessarily imply that the zero-field splitting tensors of the two sites are collinear. It implies, however, that the A- and EFG-tensors of both sites are oriented in such a way that the projections of the tensor components onto the electronic y-axis, the direction of easy magnetization for the ground doublet, are the same for both sites.
(12) Abragam, A.; Bleaney, B. *Electron Paramagnetic Resonance of Transition Ions*; Clarendon Press: Oxford, U.K., 1970.
(13) Hendrich, M. P.; Pearce, L. L.; Que, L., Jr.; Chasteen, N. D.; Day, E. P. *J. Am. Chem. Soc.* **1991**, *113*, 3039–3044.
(14) (a) Bencini, A.; Gatteschi, D. In *EPR of Spin Coupled Systems*; Springer-Verlag: New York, 1991; p 7. (b) Scaringe, R. P.; Hodgson, D. J.; Hatfield, W. E. *Mol. Phys.* **1978**, *35*, 701–713.

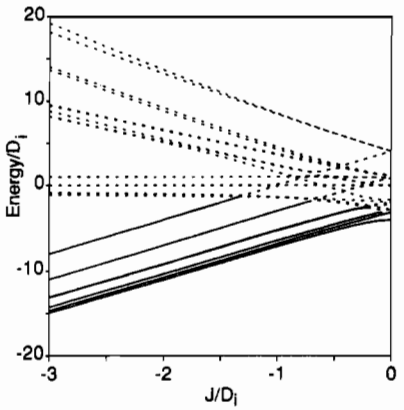

Figure 2. Energy levels of two ferromagnetically coupled $S = 2$ sites. For $|J/D_i| \gg 1$, the group of solid lines has energy spacings equivalent to an $S = 4$ site with $D = D_i/2.33$. $[Fe_2(salmp)_2]^{2-}$ has $|J/D_i| \approx 2$, producing a level spacing close to that of a pure $S = 4$ multiplet. The dashed lines are the rest of the energy levels for the ferrous pair.

least-squares fitting of the Mössbauer data. For the final presentations, however, the parameters have been converted to the uncoupled representation and all Mössbauer simulations were calculated via diagonalization of $\mathcal{H}_{SS}$ (eq 1).

Equation 1 is sufficient for describing the EPR and magnetization data. For the analysis of the Mössbauer spectra, eq 1 needs to be augmented by terms describing the hyperfine interactions of the ^{57}Fe nucleus with its electronic environment,

$$\mathcal{H}_{hf} = \sum_{i=1,2}(\mathbf{S}_i \cdot \mathbf{a}_i \cdot \mathbf{I}_i + \mathcal{H}_{Qi} - g_n\beta_n \mathbf{H} \cdot \mathbf{I}_i) \qquad (4)$$

with

$$\mathcal{H}_{Qi} = (eQV_{\zeta\zeta i}/12)[3I_{\zeta i}^2 - {}^{15}/_4 + \eta_i(I_{\xi i}^2 - I_{\eta i}^2)] \qquad (5)$$

where (ξ, η, ζ) designates the principal axis system of the EFG tensor and where $\eta_i = (V_{\xi\xi i} - V_{\eta\eta i})/V_{\zeta\zeta i}$ is the asymmetry parameter. Equation 4 is written for the uncoupled representation. For the coupled representation of eq 3, the magnetic hyperfine tensor $\mathbf{A}_i$ is related to $\mathbf{a}_i$ by $\mathbf{A}_i = \mathbf{a}_i/2$.

The Mössbauer spectra were computed in the uncoupled representation by diagonalization of

$$\mathcal{H}_T = \mathcal{H}_{SS} + \mathcal{H}_{hf} \qquad (6)$$

The magnetic splittings observed in the Mössbauer spectra reflect an effective magnetic field acting on the ^{57}Fe nucleus, $\mathbf{H}_{eff} = \mathbf{H}_{int} + \mathbf{H}$, where the internal field is given by

$$\mathbf{H}_{int} = -\langle \mathbf{S}_i \rangle \cdot \mathbf{A}_i / g_n\beta_n \qquad (7)$$

At temperatures above 25 K, the electronic spin of $[Fe_2(salmp)_2]^{2-}$ fluctuates fast on the time scale of Mössbauer spectroscopy, and the values of $\langle \mathbf{S}_i \rangle$ are obtained by calculating the thermal average over the electronic spin levels.

Mössbauer Spectroscopy. Figure 3A shows a zero-field Mössbauer spectrum of polycrystalline $[Fe_2(salmp)_2]^{2-}$ recorded at 4.2 K. The spectrum consists of a single quadrupole doublet with quadrupole splitting $\Delta E_Q = 2.56$ mm/s and isomer shift $\delta = 1.17$ mm/s. These parameters unambiguously establish that the two iron sites of the complex are high-spin ferrous. Moreover, the observation of one sharp doublet suggests that both iron sites are essentially equivalent. This is further supported by the analysis of the entire data set given below; thus, we have seen no evidence in any of the spectra for inequivalent sites. ΔE_Q was found to be nearly independent of temperature; for instance, $\Delta E_Q = 2.52$ mm/s at 200 K. The nearly temperature-independent quadrupole splitting indicates that no low-lying orbital states are significantly populated at 200 K; therefore, the spin Hamiltonian approximation should be valid for the local sites. Analysis of the temperature dependence of ΔE_Q[15] gives a lower limit of 600 cm^{-1} for the energy of the first excited state.

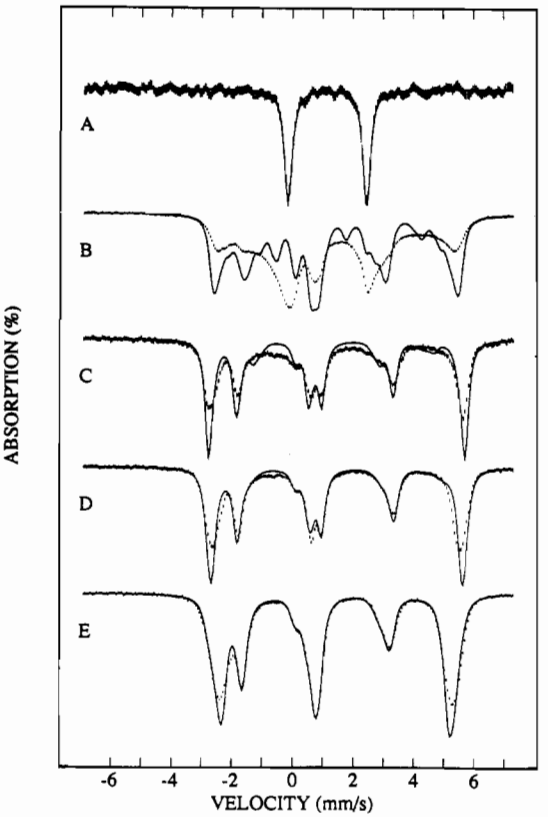

Figure 3. Variable-field Mössbauer spectra (vertical bars) and simulations (solid line) of polycrystalline $[Fe_2(salmp)_2]^{2-}$ with the magnetic field applied parallel to the γ-radiation: (A) 0 T, 4.2 K; (B) 0.25 T, 1.4 K; (C) 1.0 T, 1.4 K; (D) 3.0 T, 4.2 K; (E) 6.0 T, 4.2 K. The spectra in A, C, and D are plotted at 30%, 70%, and 70% of the normalized area, respectively. The spectra in B and C are recorded at 1.4 K to minimize relaxation effects.

The spectra shown in Figures 3B-E and 4 were recorded in the presence of a strong magnetic field applied parallel to the observed γ-radiation. The spectra of Figure 3 show that substantial magnetic hyperfine interactions have been induced already in a magnetic field of 0.25 T and that the hyperfine splitting has attained its maximal value already at 1.0 T. These features, together with the observation of sharp absorption lines, are indicative of a system with integer electronic spin which has the lowest two levels split by approximately 0.5 cm^{-1}. This situation suggests that integer spin EPR signals can be observed, as we have discussed elsewhere.[16]

We have studied $[Fe_2(salmp)_2]^{2-}$ in polycrystalline form and in acetonitrile solution. The Mössbauer spectra of the frozen solution samples were considerably broader than those observed for the polycrystalline material, presumably because of larger distributions of the zero-field splitting parameters (see below). Thus, our studies have focused on polycrystalline samples. Although the sharper features observed for polycrystalline samples were of considerable benefit, the magnetically concentrated material exhibited spin–spin interactions which persisted even at 1.5 K for applied fields below 1 T. This is clearly evident in the 0.25-T spectrum of Figure 3B which exhibits a pattern typically observed for relaxation rates that are neither fast nor slow compared to the nuclear precession frequencies. The solid line drawn in Figure 3B is a theoretical curve computed from eq 6

(15) Zimmermann, R. H.; Spiering, H.; Ritter, G. *Chem. Phys.* **1974**, *4*, 133–141.
(16) Münck, E.; Surerus, K. K.; Hendrich, M. P. *Meth. Enzymol.* **1993**, *227*, 463–479.

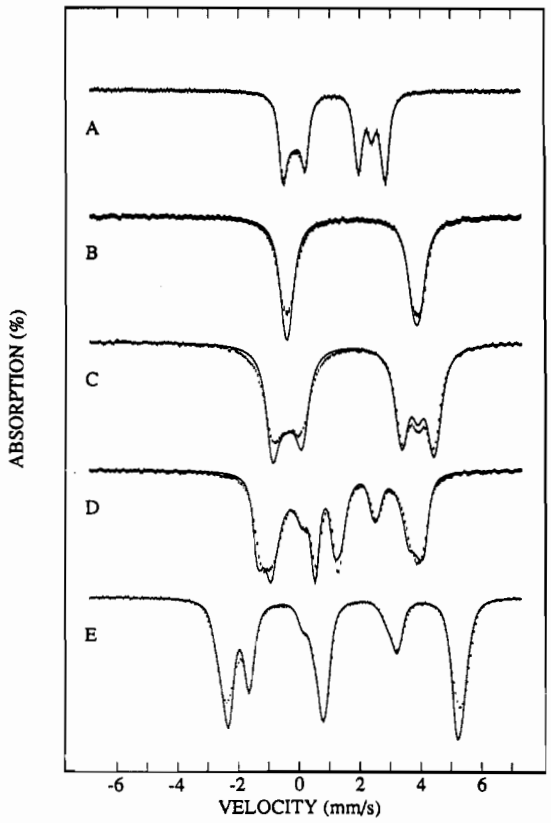

Figure 4. Variable-temperature Mössbauer spectra (vertical bars) and simulations (solid line) of polycrystalline $[Fe_2(salmp)_2]^{2-}$ at 6.0 T and (A) 150 K, (B) 74 K, (C) 50 K, (D) 25 K, and (E) 4.2 K. The spectra in A and B are plotted at 50% of the normalized area.

Table 1. Electronic and Nuclear Parameters of the Fe^{2+} Sites of Polycrystalline $[Fe_2(salmp)_2]^{2-}$ and $[Fe_2(salmp)_2]^-$

param	Fe_2^{2+}	Fe^{2+}·Fe^{3+}
J (cm^{-1})	−14	<0
D_i (cm^{-1})	+9[b]	≈+10
E_i/D_i	0.17	>0.15
$\mathbf{g}_i$	2.25, 2.30, 2.09	
$\mathbf{a}_i$ (MHz)	−20.3, −18.1, −39.8	a_y = −18.2
ΔE_Q (mm/s), η	−2.56, +0.4	−2.35, +0.3
∠EFG:**a**[a]	67, 0, 0	

[a] Euler angles $(\alpha\beta\gamma)$[17] describing the principal axis system of the EFG-tensor relative to that of the **a**-tensor. [b] D_i-value from Mössbauer spectroscopy is stated. D_i-values from EPR and magnetization measurements of solutions samples of the diferrous state gave +7 and +6 cm^{-1}, respectively, as discussed in the text.

in the slow relaxation limit with the parameter set listed in Table 1; in the fast relaxation time, the spectrum would consist of a broadened quadrupole doublet. Intermediate relaxation rates are also evident in the 1.0- and 3.0-T data.

A common cause of broadening in strong-field Mössbauer spectra is a spread (strain) of the zero-field splitting parameters D and E about their mean values. Such distributions cause a spread in the expectation values of the electronic spin, which, in turn, produces a spread in the magnetic hyperfine splittings. The widths of the absorption lines observed at 1.0 and 3.0 T can be attributed only to a minor extent to strain. This follows from an analysis of the line shapes of the EPR spectra which yield information about the spreads in D and E. The EPR data discussed below suggest that at most 30% of the increased width at 1.0 and 3.0 T can be attributed to strain broadening. At 6.0 T, the spin–spin interactions are not relevant because only the lowest electronic state is appreciably populated at 4.2 K.

By the appropriate scaling of the magnetic hyperfine tensors in eq 1, the low-temperature Mössbauer spectra could be fitted in the limit of strong exchange coupling, $|J| \gg |D_i|$, as well as in the limit of $J = 0$. However, when these results were applied to the high-temperature data of Figure 4, the computed magnetic hyperfine splittings were too large for the strong coupling case and too small for the uncoupled case; i.e. the system reflects a situation where the exchange coupling is comparable to the zero-field splitting and where more than one multiplet is populated at higher temperatures. Moreover, at 0.25 T the low-temperature Mössbauer spectra show a substantial magnetic broadening, indicating that the coupling must be ferromagnetic.

The field dependence of the magnetic hyperfine splittings observed at $T \leq 4.2$ K can be used to determine D and E/D. From the fits of the spectra in Figure 3, the zero-field splitting parameter D of eq 3 must be positive and E/D must be near midrange of its allowed values $0 \leq E/D \leq 1/3$. The six-line patterns observed at 1.0 and 3.0 T shows that for $D > 0$ the y-direction is the axis of easy magnetization, i.e. $|\langle S_y \rangle| \gg |\langle S_x \rangle|, |\langle S_z \rangle|$ for the lowest two levels of the spin manifold.

Figure 4 shows a series of 6.0-T spectra recorded in the temperature range from 4.2 K to 150 K. Comparison of the spectra in Figure 4D,E shows that the electronic spin fluctuates fast compared to the nuclear precession frequencies for $T \geq 25$ K. The thermal expectation value of the electronic spin, $\langle S_i \rangle_{th}$, depends on the values of J, D_i, E_i, and the electronic $\mathbf{g}_i$-tensors of the two sites. It can be seen that the magnetic splitting decreases as the temperature is raised above 4.2 K. At 74 K, the magnetic splittings have almost vanished because the negative internal magnetic field is nearly compensated by the 6.0-T applied field. With a further increase of the temperature, the applied field becomes larger than the internal fields (which are proportional to $1/T$) and a sizable magnetic splitting is observed. The splitting pattern observed at 150 K shows that $\Delta E_Q < 0$; i.e., the largest component of the EFG-tensor is negative. Our analysis of the low- and high-temperature data shows that the asymmetry parameter η is restricted to $0.2 < \eta < 0.5$. Moreover, the low-temperature data show that the ζ-axis of the EFG-tensor is parallel to the electronic z-axis. This implies for the spectra of Figure 4A-D that the splittings of the low-energy bands (velocity < 0) is determined by $\langle S_z \rangle_{th}$ and A_z while those of the high-energy bands are primarily determined by the corresponding x- and y-components. Thus, the variable-temperature Mössbauer spectra convey information similar to that obtainable from single-crystal magnetization studies.

The solid lines in Figures 3 and 4 are theoretical curves generated from eq 6 with the parameters listed in Table 1. The entire data set was fitted with the same parameters. Given the relaxation problems affecting the spectra of Figure 3B-D, the overall agreement between theory and experiment is very good. Clearly, individual spectra can be fit better. For example, a 1.5% reduction of A_z will match the splittings of the theoretical curves with the data of Figure 3C,D. Alternatively, one could achieve a better fit to these spectra by postulating slightly inequivalent sites, in accord with the X-ray data, to account for the broader outer lines.

EPR Spectroscopy. X-band EPR spectra of $[Fe_2(salmp)_2]^{2-}$ dissolved in acetonitrile are shown in Figure 5 for orientations of the microwave field $\mathbf{H}_1$ parallel and perpendicular to the static field $\mathbf{H}$. The perpendicular mode spectrum (Figure 5C) shows a valley at $g = 19$ ($g = h\nu/\beta H$), which in parallel mode (Figure 5B) sharpens, intensifies, and shifts to $g = 26$. The absorption EPR spectrum obtained from integration of the parallel mode spectrum is shown in Figure 5A. The spectrum shows finite intensity at zero field due to a fraction of molecules which have two levels split in energy by $\Delta = h\nu \approx 0.3$ cm^{-1}. The temperature dependence of the signal, measured by the depth of the resonance at $g = 26$, is shown in Figure 6. The signal intensity is largest

(17) Brink, P. M.; Satchler, G. R. *Angular Momentum*; 2nd ed.; Clarendon Press: Oxford, U.K., 1979; p 20.
(18) The EPR spectra of this doublet are insensitive to g_x and g_z.

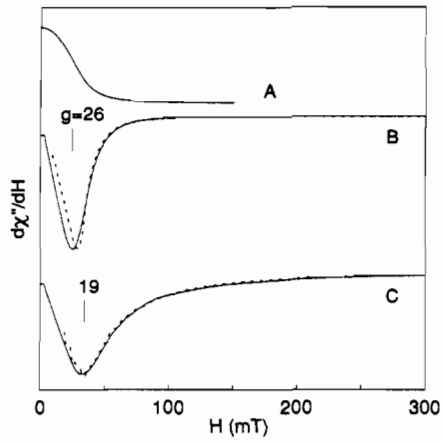

Figure 5. X-band EPR spectra (solid line) and simulations (dashed line) of 5 mM $[Fe_2(salmp)_2]^{2-}$ in acetonitrile recorded with (B) $\mathbf{H}_1$ parallel to **H** and (C) $\mathbf{H}_1$ perpendicular to **H**. The absorption spectrum A is a digital integration of (B). Simulation parameters: $S = 4$, $D = 2.8$ cm^{-1}, $\sigma_D = 0.4$ cm^{-1}, $E = 0.4$ cm^{-1} ($E/D = 0.14$), $\sigma_E = 0.06$ cm^{-1}, and $g_{cy} = 2.25$.[18] Instrumental parameters: temperature, 4 K; microwaves, 0.02 mW at 9.081 GHz (B), 9.138 GHz (C); modulation, 1 mT_{pp} at 100 kHz; gain, 3200.

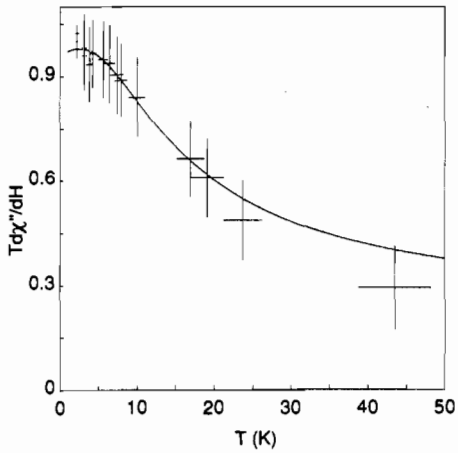

Figure 6. Temperature dependence of the X-band signal at 25 mT in Figure 5B. The solid line is a theoretical curve for the lowest doublet of an $S = 4$ multiplet with parameters $D = 2.8$ cm^{-1} and $E/D = 0.23$ (see text regarding the magnitude of E/D).

at 2.5 K, the lowest temperature employed, and the signal begins to broaden near 50 K. The plot of (signal intensity)·T versus T shows a continuous decrease as the temperature is increased, indicating that the doublet giving the EPR signal is lowest in energy and is depopulated by low-lying excited energy levels.

A Q-band spectrum of $[Fe_2(salmp)_2]^{2-}$ in acetonitrile is shown in Figure 7. The signal, observed with $\mathbf{H}_1$ perpendicular to **H**, has a zero crossing at $g = 17$. The resonance at $g = 6.4$ is preparation-dependent and accounts for <5% of the total iron; it is attributed to an Fe^{3+} impurity species.

The above EPR signals exhibit features which are typical for a resonance between energy levels of an integer spin multiplet, namely an enhanced parallel mode signal, a frequency-dependent line shape, and a residual signal intensity at zero field. The likely multiplets which would give rise to these signals are either an $S = 2$ manifold of high-spin Fe^{2+} or a multiplet derived from an exchanged-coupled pair of high-spin Fe^{2+} sites. Thus, an analysis of these signals will follow previous studies of mononuclear[8] and binuclear[13,19] iron sites. Three main steps in the analysis are to be discussed next.

First, the magnitude of S can be determined from spectra at two different microwave frequencies and, thus, whether a

(19) Hendrich, M. P.; Münck, E.; Fox, B. G.; Lipscomb, J. D. *J. Am. Chem. Soc.* **1990**, *112*, 5861–5865.

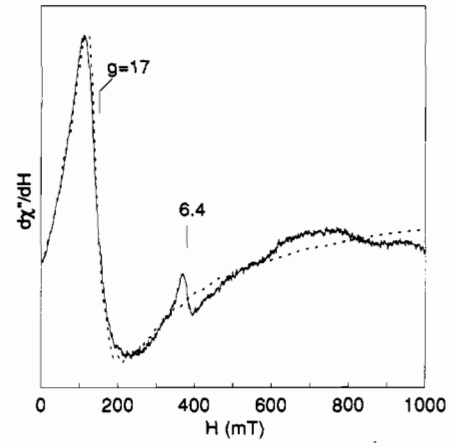

Figure 7. Q-band EPR spectrum (solid line) and simulation (dashed line) of 5 mM $[Fe_2(salmp)_2]^{2-}$ in acetonitrile recorded with $\mathbf{H}_1$ perpendicular to **H**. The simulation parameters are the same as those given in Figure 5. Instrumental parameters: temperature, 5 K; microwaves, 0.3 mW at 34.1 GHz; modulation, 1 mT_{pp} at 100 kHz; gain, 1250.

mononuclear or binuclear site is involved. The resonance condition for integer spin EPR signals is

$$(h\nu)^2 = \Delta^2 + (g_{eff}\beta H \cos\theta)^2 \qquad (8)$$

where Δ is the zero-field splitting of the doublet, g_{eff} is the effective g-value along a principal axis of the zero-field coordinate frame, and θ is the angle between that principal axis and the static field **H**. There are two unknown parameters in eq 8, Δ and g_{eff}, that reflect properties of the complex. These parameters are uniquely determined from simultaneous simulations of the spectra, from which we find $g_{eff} = 18$ for $[Fe_2(salmp)_2]^{2-}$. The maximum g-value for all doublets of a multiplet having spin S is $g_{eff} = 2g_cS$, where $2 < g_c < 2.3$ of eq 3. The above EPR signals can not originate from an $S = 2$ mononuclear Fe^{2+} site because $g_{eff} \approx 8$ for this multiplet. However, they can originate from an $S = 4$ multiplet ($g_{eff} \approx 16$) of an exchanged-coupled diferrous cluster.

Second, the D-value of the $S = 4$ multiplet can be determined by fitting the temperature dependence of the signal with eq 3. The fit for $D = 2.8$ cm^{-1} is shown in Figure 6. It is important to note that this step and the third step to follow are not totally independent. As will be discussed below, the X-band signal represents a relatively small subset of the molecules in any given sample of $[Fe_2(salmp)_2]^{2-}$. Thus, the parameters obtained from the fit of Figure 6, D and E/D, are in a wing of a distribution of parameters that best characterizes the complex. For example, from the fit of Figure 6 we have $E/D = 0.23$, but the simulations of both the X- and Q-band spectra provide a better measure to give $E/D = 0.14$ (see below).

Third, simulations of the spectra of Figures 5 and 7 afford both a quantitative determination of spin concentration and a determination of the remaining unknown zero-field splitting parameters. The simulations shown in both figures use a single parameter set, which is given in the caption of Figure 5. The X-band perpendicular mode spectrum is predicted from the parallel mode simulation without adjustment of the zero-field splitting parameters or intensity. The D_i-value and distribution width expressed in the uncoupled representation of eq 1 are $D_i = 6.5$ cm^{-1} and $\sigma_D = 0.9$ cm^{-1}.[20]

The simulations were generated with the assumption that the dominant source of line broadening is a spread in the zero-field splitting parameters.[8] This spread presumably originates from

(20) The $S = 4$ multiplet has with 98% of the spin population at $T = 25$ K. Thus, the temperature dependence shown in Figure 6 is not appreciably affected by the excited $S = 3$ multiplet.

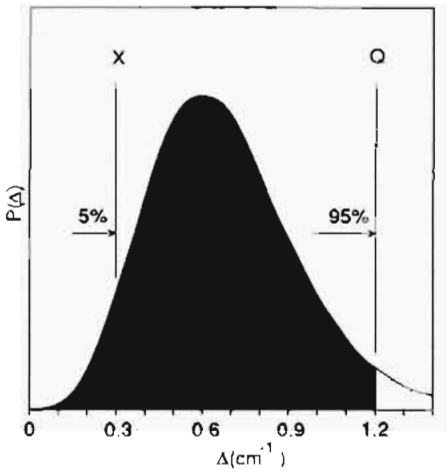

Figure 8. Probability distribution of Δ-values for the ground doublet of the $S = 4$ multiplet of $[Fe_2(salmp)_2]^{2-}$ in acetonitrile. The deconvolution was computed from the parameters given in Figure 5. Molecules with $\Delta < 0.3$ cm^{-1} or $\Delta < 1.2$ cm^{-1} contribute to the X- or Q-band signal intensity, respectively.

small random variations in the bond lengths and angles of the coordination units of the two Fe^{2+} atoms. These variations modulate the orbital energies and, via spin–orbit coupling, result in spreads of the zero-field splitting parameters. The simulations assume Gaussian distributions in D- and E-values. We have assumed for simplicity that the distribution widths σ_D and σ_E are related in magnitude by $\sigma_D/D = \sigma_E/E$. This assumption is not critical; equally good simulations are obtained with smaller σ_D and a commensurate increase in σ_E. These distributions in D- and E-values result in a broad spread in the Δ-values of the EPR-active spin doublet. This distribution can be determined from the simulations of the $[Fe_2(salmp)_2]^{2-}$ EPR data and is shown in Figure 8. The distribution is centered at $\Delta \approx 0.6$ cm^{-1}. The fraction of molecules which contributes to the intensity of the X-band EPR spectrum, i.e. those molecules with $\Delta < 0.3$ cm^{-1}, is only a 5% wing in Figure 8. A much larger fraction of the molecules (95%) are observed in the Q-band EPR spectrum ($\Delta < 1.2$ cm^{-1}). Thus, the Q-band spectra give a significantly better reflection of the magnetic properties of $[Fe_2(salmp)_2]^{2-}$. Ideally, the analyses should rely most heavily on data obtained from Q-band EPR spectroscopy; however, these data are of poor quality owing to instrumentation difficulties yet to be overcome, including poor sensitivity, unstable baselines, and the inability to align $\mathbf{H}_1$ parallel with $\mathbf{H}$.

The spin concentration of the sample can be determined from the EPR spectra.[8] This requires that we know the intrinsic spectral intensity of the EPR signal of $[Fe_2(salmp)_2]^{2-}$ and the instrumental intensity constant. The former is determined from spectral simulations of Figure 5, and the latter is determined from a spin standard of known concentration. From this procedure, the concentration of $[Fe_2(salmp)_2]^{2-}$ in acetonitrile was found to be within 50% of that determined spectrophotometrically. The unusually large error is due to inaccuracies which are introduced by the Q-band data. If instead we base the quantification on simulations which give perfect matches to only the X-band spectra of Figure 5,[21] then the difference between the EPR and optical values of the iron cluster concentration was found to be 5%.

Magnetism. Saturation magnetization data for a concentrated solution of $[Fe_2(salmp)_2]^{2-}$ in acetonitrile are presented in Figure 9. The data were collected over the temperature range 2–200 K at four fields between 0.2 and 5.5 T and fit to eq 1 with the assumption of two identical, collinear high-spin ferrous sites. The solid curves were calculated with $D_i = 6.1$ cm^{-1}, $E_i/D_i = 0.17$, isotropic $g_i = 2.21$, and $J = -14.0$ cm^{-1}. The concentration of the Fe^{2+}·Fe^{2+} dimer was treated as a free parameter. The amount of dimer in the 100-μL sample was found to be 0.61 μmol.

(21) These simulations are not shown because they precisely overlap the X-band spectra.

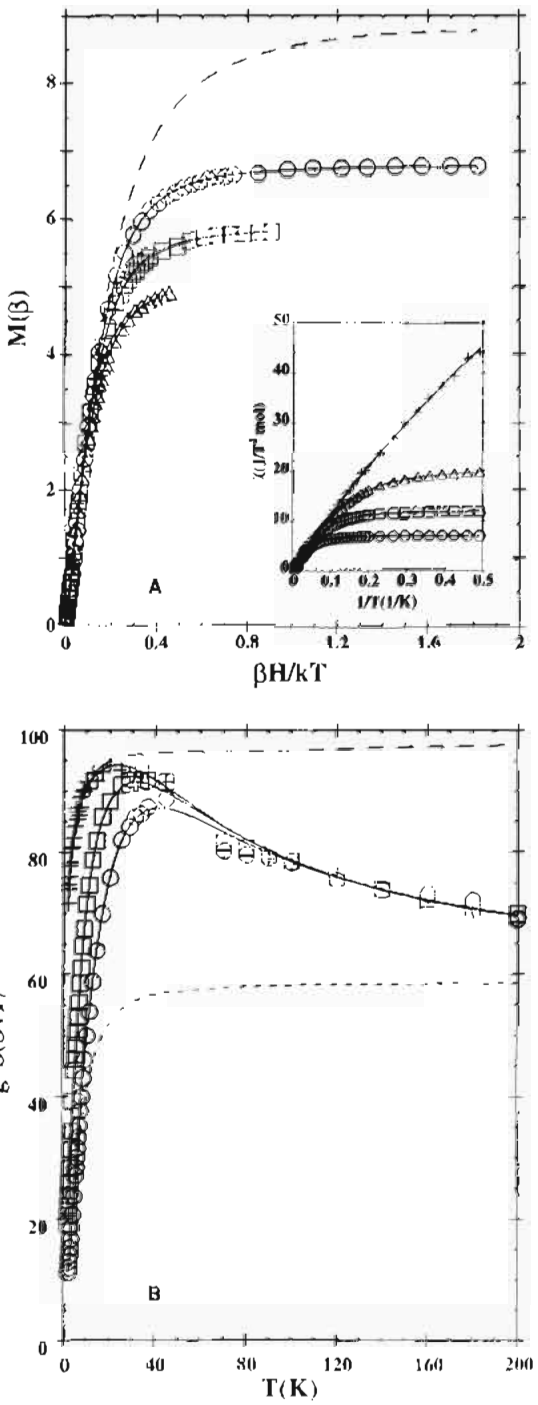

Figure 9. Saturation magnetization data of $[Fe_2(salmp)_2]^{2-}$ in acetonitrile. The data were taken at fixed fields of (○) 5.5 T, (□) 2.75 T, (△) 1.375 T, and (+) 0.2 T. The solid lines were calculated from eq 1 assuming two identical, collinear, $S = 2$ sites with $D_i = 6.1$ cm^{-1}, $E_i/D_i = 0.17$, isotropic $g_i = 2.21$, and $J = -14.0$ cm^{-1} ($\chi^2 = 1.0$). (A) Top: Plot of the magnetization in Bohr magnetons (β) versus $\beta H/kT$. The dashed line is the Brillouin curve for $S = 4$, calculated with $D = E = 0$ for $g_c = 2.21$. The low-temperature asymptote of the Brillouin curve is 8.83β for $g_c = 2.21$. The inset presents the same data and fit plotted as susceptibility ($\chi = M/H$) in molar SI units versus temperature. (B) Bottom: Same data and fit (1.375-T data omitted for clarity) are plotted as $g^2S(S+1)$ versus temperature. The long and short dashed lines are limiting curves calculated with $J = -\infty$ ($H = 0.2$ T) and $J = 0$ ($H = 5.5$ T), respectively.

To estimate the uncertainties in the magnetization parameters, we fit the magnetization data in three different ways using the same number of free parameters in each case. First, we assumed

that no impurities were present. This gave $\chi^2 = 1.7$, indicating an excellent fit.[22] Second, we fit the data by assuming that a fraction of the sample was present in the diferric form ($J = -3.2$ cm^{-1}, $D_i = -0.3$ cm^{-1}; unpublished results). The presence of such a contaminant was evident in some samples studied with Mössbauer spectroscopy. For this fit we locked the value of E_i/D_i of the diferrous complex at 0.17 and locked all electronic parameters of the diferric state at the values found from a direct study of that state. This gave the best fit, with $\chi^2 = 1.0$ and a 6% diferric impurity. The data in Figure 9 were obtained by subtracting this diferric impurity from the raw data. Third, we fit the data with the assumption that the sample contained a small amount of adventitious high-spin Fe^{3+}. Both EPR and Mössbauer gave evidence of this impurity in some samples. This gave $\chi^2 = 1.6$ and a 2% ferric impurity. Averaging the results of these three fits gives $D_i = 5.5(9)$ cm^{-1}, $E_i/D_i = 0.17$, $g_i = 2.26(4)$, and $J = -13.7(4)$ cm^{-1} for $[Fe_2(salmp)_2]^{2-}$.

Figure 9A shows a plot of the magnetization versus $\beta H/kT$. For comparison we have drawn a Brillouin curve (dashed line) computed for $S = 4$ and isotropic $g_c = 2.21$. A Brillouin curve is calculated under the assumption that $D = E = 0$. Thus, the deviation of the experimental data from the Brillouin curve highlights the effects of the zero-field splitting. Because $g_c = 2.21$, the low-temperature asymptote of the Brillouin curve of Figure 9A is 8.83β (rather than the 8β expected for spin $S = 4$ with $g_c = 2$). The inset of Figure 9A presents the same data and fit plotted as susceptibility ($\chi = M/H$) in molar SI units against inverse temperature to illustrate the quality of the fit at low temperatures at each of the fixed fields. The same data and fit (with the 1.375-T data omitted for clarity) are plotted as $g^2S(S + 1)$ against temperature in Figure 9B to highlight the quality of the data and fit at high temperature. The fact that the data in Figure 9B rise with decreasing temperature below 200 K indicates ferromagnetic coupling. The long-dashed line was calculated assuming $J = -\infty$ ($H = 0.2$ T) and indicates μ_{eff}^2 for an $S = 4$ state. This curve and the $J = -14$ cm^{-1} curve (solid line) diverge for temperatures above 20 K due to population of the low-lying $S = 3$ multiplet. The short-dashed line was calculated with $J = 0$ ($H = 5.5$ T, $g_i = 2.21$) and indicates μ_{eff}^2 for two uncoupled $S = 2$ centers. The high-temperature asymptote is 58.5, which equals the value of μ_{eff}^2 for two $S = 2$ paramagnets with $g_i = 2.21$.

Fits of the quality shown in Figure 9 to multifield saturation magnetization data are quite uncommon in the literature. When the data are handled properly and fit in this manner, it is possible to determine from the magnetization data alone whether or not the sample is magnetically pure.[10] When the sample is essentially pure (as is the case for the data shown in Figure 9), the spin (S), spin concentration ($[S]$), g value, zero-field splitting parameters ($D, E/D$), and exchange coupling (J) can be determined from the multifield saturation magnetization data alone without knowing the concentration of the compound being studied. In particular, there will be no ambiguity in the spin. On the other hand, from saturation magnetization data taken at a single field one cannot even determine the spin.[10]

The magnitude of the exchange coupling found here ($J = -13.7$ cm^{-1}) from fitting the multifield saturation magnetization data to eq 1 is 5.5 times larger than the value previously reported ($J = -2.46$ cm^{-1}).[5] The smaller magnitude found previously was based on a fit to data taken at a single field (0.5 T) over a higher temperature range (6–300 K) using a model which neglected the zero-field splittings. Our study indicates an error in the previously published value of the exchange coupling of $[Fe_2(salmp)_2]^{2-}$. When we fit the published data of both the diferric and the mixed-valence states under the assumption $D_i = E_i = 0$, we arrive at J-values similar to the published values. However, from a fit to the published data of the diferrous state, we obtain a substantially larger J-value which is near -14 cm^{-1}. We also find that for the three oxidation states of $Fe_2(salmp)_2$, the J-values derived from van Vleck fits (single field with $D_i = E_i = 0$) only slightly underestimate the J-values obtained from multifield fits using the full spin Hamiltonian $\mathcal{H}_{SS}$ (eq 1).

(22) $\chi^2 = \sum_i (\text{resid}_i)^2 W_i/N$, where W_i is a weighting factor for the ith point and N is the number of data points (300). See ref 10 for further details.

Discussion

This study of $[Fe_2(salmp)_2]^{2-}$ has provided an opportunity to explore methods for analysis of diferrous complexes and to characterize the electronic properties of this complex in detail. The electronic properties of a few diferrous complexes have been reported, and we will show here that $[Fe_2(salmp)_2]^{2-}$ has some unique properties. It is a crystallographically characterized complex which affords relatively well-defined spectroscopic features. The two Fe^{2+} sites are indistinguishable by Mössbauer spectroscopy, a fact not obvious from inspection of the crystal structure. The presence of equivalent Fe^{2+} sites allows for simplification of a complex multivariable problem because we may assume that both sites have equal and collinear $\mathbf{D}_i$-, $\mathbf{g}_i$-, $\mathbf{a}_i$-, and EFG-tensors. With this assumption, a consistent and quantitative description of the properties of $[Fe_2(salmp)_2]^{2-}$ has been achieved through, in most respects, independent analyses of the EPR, Mössbauer, and magnetization data. Most importantly, we have been able to fit the data over a whole range of temperatures and applied fields to a spin Hamiltonian. To our knowledge, this is the first instance for which this has been accomplished for a spin-coupled diferrous system.

Magnetization measurements and Mössbauer spectroscopy both yield $J = -14$ cm^{-1} for the exchange-coupling constant; EPR probes mainly the lowest levels of the $S = 4$ multiplet and is thus not sensitive to the value of J in this case. The D_i-values determined from Mössbauer (9 cm^{-1}), EPR (7 cm^{-1}), and magnetization (6 cm^{-1}) studies differ appreciably but not outside of realistically estimated uncertainties of ± 2 cm^{-1}. EPR conducted with helium gas-flow systems always suffers from uncertainties in temperature determination and temperature gradients that develop across the samples. More importantly, our EPR studies have revealed substantial spreads of the zero-field splitting parameters. Thus, some variation in the D_i-values obtained may be due to each technique sensing a different average of this distribution. For instance, we have shown above that X-band EPR is sensitive only to those molecules in the sample which have $\Delta < 0.3$ cm^{-1} (5% of the total; see Figure 8). Moreover, the relative population within the distribution of Figure 8 will change with temperature because molecules with different Δ-values have different level sequences. Magnetization studies are generally conducted with precise temperature control but are affected by paramagnetic contaminants and insensitivity to distributed parameters. We have observed with Mössbauer spectroscopy that some solution samples contain (up to 15%) diferric contaminants as well as mononuclear high-spin Fe^{3+}. In this study, we have accounted for the presence of these contaminants in the fits of the magnetization data. Our Mössbauer studies were conducted on polycrystalline material that exhibited orientation-dependent spin–spin relaxation under conditions (0.5–2.0-T applied field) where the data would be most sensitive to the value of D_i. The spin–spin relaxation effects are indicative of lattice exchange couplings that may artificially inflate the D_i-values. One might also be inclined to attribute the larger D_i-value obtained by Mössbauer spectroscopy to differences in polycrystalline and solution properties of the samples.[23] However, the ΔE_Q and δ values were found to be the same for solution and polycrystalline samples, and their 6.0-T Mössbauer spectra were essentially the same. In summary, the value $D_i = 7 \pm 2$ cm^{-1} accommodates the results obtained by the three techniques.

Table 2. *J*-Values of Diferrous Complexes Having One or Two Single Atom Bridges

Fe–X–Fe[a]	∠Fe–X–Fe	J (cm^{-1})[b]	ref
tacn (OH^-)	113.2	+22	24
bpmp (PhO^-)	122.7	+1.5 (zfs)	25
biphme ($-CO_2^-$)	113.1	~0	26
hptb (alkoxo)	124.0	+22	27
tmen (H_2O)	112.8	~0	28
deoxyHr (OH^-)	128	+24 to +76 (zfs)	29
deoxyHrN_3 (H_2O)		−3 (zfs)	13
MMOH		<0 (zfs)	19
RNR N_3 (H_2O)		<0	30
Fe(X)Fe[a]	**∠Fe–X–Fe**	**J (cm^{-1})[b]**	**ref**
salmp (PhO^-)	96	−14 (zfs)	*c*
tpza (Cl^-)	91.9	−3 (zfs)	31
tla (F^-)	101.7	−1 (zfs)	31
tpa (Cl^-)	90.7	−10 (zfs)	31
$h_2$hbab (PhO^-)	98.9	−5	32
tthd (PhO^-)	93.3	+3 to +15	33

[a] Ligands are polydentate with O/N binding sites; for ligand structures corresponding to the abbreviations, see references cited. The bridge component is given in parentheses. [b] $\mathcal{H}_{ex} = JS_1 \cdot S_2$. zfs indicates that zero-field splittings were included in the determination of the *J*-value. [c] This work.

A list of relevant proteins and synthetic complexes and their reported exchange couplings is presented in Table 2. Thus far, $[Fe_2(salmp)_2]^{2-}$ has the largest ferromagnetic *J*-value of oxygen-bridged diferrous clusters. For most of the complexes listed, not only is the range of *J*-values relatively small, but the magnitude of *J* is comparable to the zero-field splitting of Fe^{2+} ($|D| \lesssim 10$ cm^{-1}). As indicated above for $|J| \geq |D_i|$, one can obtain reasonably precise *J*-values from magnetization studies even without consideration of the zero-field splitting parameters. For $|J| \leq 10$ cm^{-1}, on the other hand, knowledge of the zero-field splitting parameters is mandatory if reliable *J*-values are to be obtained. In this case, the reader should be aware that *J*-values determined without taking into account zero-field splittings may give misleading magneto–structural correlations.

Although only a few *J*-values are available from complexes with known structures, the coupling constants of the clusters in Table 2 appear to correlate with the number of single atom bridges. The coupling of the Fe^{2+}–X–Fe^{2+} type clusters tends to be antiferromagnetic, whereas bis-bridged clusters seem to favor ferromagnetic coupling. This variation in the exchange coupling is often rationalized on the basis of the Fe–X–Fe angle. Angles close to 90° promote ferromagnetic exchange couplings, because the p-orbitals of the bridging atom X which overlap with the magnetic orbitals of one iron are orthogonal to the magnetic orbitals of the other iron.[14a] Bis-bridged clusters have smaller Fe–X–Fe angles as can be seen from inspection of Table 2. Thus, the exchange couplings of bis-bridged clusters tend to be ferromagnetic. Another factor may well be as important in determining the strength of the exchange coupling. For bis-bridged clusters there are two important exchange pathways, one through each of the bridging atoms X, that could potentially contribute to the exchange coupling. However, if the orbitals involved in these two pathways are of opposite symmetry, a net cancellation of the antiferromagnetic contribution from each pathway can occur, as has been previously observed in a $Cu^{2+} \cdot VO^{2+}$ complex.[34] The crystallographic symmetry of $[Fe_2(salmp)_2]^{2-}$ is rhombic or lower, which mitigates such cancellation effects. Nevertheless, both the Fe–X–Fe angle and symmetry considerations may conspire to give ferromagnetic exchange couplings in bis-bridged complexes.

Correlation with the Mixed-Valence Complex $[Fe_2(salmp)_2]^-$. The mixed-valence form of $Fe_2(salmp)_2$ has been studied previously.[5,6] The EPR, Mössbauer, and magnetization data all show that the $Fe^{3+} \cdot Fe^{2+}$ pair is ferromagnetically coupled to give a ground $S = {}^9/_2$ multiplet. In a spin-coupling model, the parameters of this multiplet can be related to those of the individual iron sites by

$$\mathbf{D}_{9/2} = (5\mathbf{D}_3 + 3\mathbf{D}_2)/18$$

$$\mathbf{g}_{9/2} = (5\mathbf{g}_3 + 4\mathbf{g}_2)/9 \qquad (9)$$

$$\mathbf{A}_{9/2}^{(3)} = ({}^5/_9)\mathbf{a}_3 \qquad \mathbf{A}_{9/2}^{(2)} = ({}^4/_9)\mathbf{a}_2$$

where the indices 2 and 3 refer to the ferrous and ferric sites, respectively. The *D*-values of ferric sites are generally much smaller than those of ferrous sites;[35] our magnetization studies of the mixed-valence complex of $Fe_2(salmp)_2$ (unpublished) suggest $D_3 \approx 0.5$ cm^{-1}. Therefore, to simplify the problem we may set $D_3 = 0$. Using the experimental values[6] $D_{9/2} \approx 1.5$ cm^{-1} and $A_y^{(2)} = 8.1$ MHz, the parameters of the ferrous site of the mixed-valence complex are calculated with eq 9 and listed in Table 1. We find that the parameters describing the ferrous site of the mixed-valence state are close to those of the diferrous state, indicating that the electronic properties of the ferrous site of the mixed-valence form do not significantly change upon reduction of the ferric site.

Ligand Field Analysis. The Fe^{2+} sites of all the oxygen-bridged iron proteins and synthetic complexes reported thus far have $\Delta E_Q > 0$. For a pure t_{2g}-orbital, the largest component of the EFG-tensor is positive, i.e. $\Delta E_Q > 0$. The complexes $[Fe_2(salmp)_2]^{2-,1-}$ are the first examples of oxygen-bridged systems which have a Fe^{2+} site with $\Delta E_Q < 0$. Since the ΔE_Q of $[Fe_2(salmp)_2]^{2-}$ is essentially independent of temperature, the splitting of the t_{2g}-levels is significantly larger than the spin–orbit coupling energy. Therefore, mixing of t_{2g}-orbitals by spin–orbit coupling will not give $\Delta E_Q < 0$; however, a suitable geometric distortion of the octahedral environment can produce $\Delta E_Q < 0$.[36] Therefore, we present here a ligand-field analysis of the Fe^{2+} sites of $Fe_2(salmp)_2$ to assess the composition of the ground orbital state and the electronic symmetry of the iron sites.

(23) Ideally, the three techniques should be applied to the same sample. This is generally not practical because EPR spectroscopy has special sample holder requirements. One therefore may want to study samples at least from the same batch. The current studies have been carried out, somewhat independently, at four different locations. During our studies a variety of problems had to be overcome or avoided, such as sublimation of solvents in the susceptometer, heterogeneous broadening of Mössbauer absorption lines for frozen solution samples, and spin–spin interactions in solid samples or concentrated solutions. In order to avoid some of these problems, we have optimized the requirements for each technique and studied samples from different batches in different physical states.

(24) Hartman, J. R.; Rardin, R. L.; Chaudhuri, P.; Pohl, K.; Wieghardt, K.; Nuber, B.; Weiss, J.; Papaefthymiou, G. C.; Frankel, R. B.; Lippard, S. *J. Am. Chem. Soc.* **1987**, *109*, 7387–7396.
(25) Jang, H. G.; Hendrich, M. P.; Que, L., Jr. *Inorg. Chem.* **1993**, *32*, 911–918.
(26) Tolman, W. B.; Schuncheng, L.; Bentsen, J. G.; Lippard, S. J. *J. Am. Chem. Soc.* **1991**, *113*, 152–164.
(27) Ménage, S.; Brennan, B. A.; Juarez-Garcia, C.; Münck, E.; Que, L., Jr. *J. Am. Chem. Soc.* **1990**, *112*, 6423–6425.
(28) Hagen, K.; Lachicotte, R. *J. Am. Chem. Soc.* **1992**, *114*, 8741–8742.
(29) Reem, R. C.; Solomon, E. I. *J. Am. Chem. Soc.* **1987**, *109*, 1216–1226.
(30) Elgren, T. E.; Hendrich, M. P.; Que, L., Jr. *J. Am. Chem. Soc.* **1993**, *115*, 9291–9292.
(31) Zang, Y.; Jang, H. G.; Chiou, Y.-M.; Hendrich, M. P.; Que, L., Jr. *Inorg. Chim. Acta* **1993**, *213*, 41–48.
(32) Stassinopoulos, A.; Schulte, G.; Papaefthymiou, G. C.; Caradonna, J. P. *J. Am. Chem. Soc.* **1991**, *113*, 8686–8697.
(33) Spiro, C. L.; Lambert, S. L.; Smith, T. J.; Duesler, E. N.; Gagne, R. R.; Hendrickson, D. N. *Inorg. Chem.* **1981**, *20*, 1229–1237.
(34) Kahn, O.; Galy, J.; Journaux, Y.; Jand, J.; Morgenstern-Babarau, I. *J. Am. Chem. Soc.* **1982**, *104*, 2165–2176.
(35) (a) Juarez-Garcia, C.; Hendrich, M. P.; Holman, T. R.; Que, L., Jr.; Münck, E. *J. Am. Chem. Soc.* **1991**, *113*, 518–525. (b) Beck, J. L.; de Jersey, J.; Zerner, B.; Hendrich, M. P.; Debrunner, P. G. *J. Am. Chem. Soc.* **1988**, *110*, 3317–3318.
(36) Cosgrove, J. R.; Collins, R. L. *J. Chem. Phys.* **1971**, *55*, 4238–4245.

The fine and hyperfine parameters of eq 1 can be derived from the Hamiltonian

$$\mathcal{H} = \mathcal{H}_{free} + \mathcal{H}_{LF} + \mathcal{H}_{SO} + \mathcal{H}_{Z} + \mathcal{H}_{HF} \qquad (10)$$

where $\mathcal{H}_{free}$ contains the kinetic, central field, and electron–electron repulsion interactions of the free Fe^{2+} ion and $\mathcal{H}_{SO}$, $\mathcal{H}_{Z}$, and $\mathcal{H}_{HF}$ describe the spin–orbit coupling, the electronic Zeeman interaction, and the hyperfine interaction, respectively.[12] High-spin Fe^{2+} obeys Hund's rules, and the application of $\mathcal{H}_{free}$ results in a ^5D ground orbital term state. We consider the ligand-field potential

$$\mathcal{H}_{LF} = \sum_{i=1,6}[C_4(x_i^4 + y_i^4 + z_i^4 - (^3/_5)r_i^4) + B_2^{(0)}(3z_i^2 - r_i^2) + B_2^{(2)}(x_i^2 - y_i^2)] \qquad (11)$$

where C_4 describes the cubic-field splitting and $B_2^{(0)}$ and $B_2^{(2)}$ are the magnitudes of the tetragonal and rhobmic distortions of the cubic field, respectively, and the sum is over the six valence electrons.

For $[Fe_2(salmp)_2]^{2-}$, ΔE_Q is nearly temperature independent, which indicates that the first excited orbital state is at least 600 cm^{-1} above the ground state. Therefore, the terms in the Hamiltonian that depend on the electronic spin S can be treated with perturbation theory. For our calculation, we have used a computer program, written by Champion,[37] that calculates the $\mathbf{D}_i$-, $\mathbf{g}_i$-, $\mathbf{a}_i$-, and EFG-tensors and their orientations relative to the cubic coordinate frame, for a set of ligand-field parameters C_4, $B_2^{(0)}$, $B_2^{(2)}$, and Euler angles $(\alpha\beta\gamma)$. To approximate symmetries other than tetragonal, the program allows a general rotation $(\alpha\beta\gamma)$ of the axial and rhombic distortions relative to the cubic frame.

A solution and its corresponding calculated spin Hamiltonian parameters are listed in Table 3. For a ligand-field parameter set to be deemed a solution, it must simultaneously predict, within experimental errors, D_i, E_i/D_i, g_{iy}, $\Delta E_Q < 0$,[38] and η of Table 1. In order to reduce ambiguities, we have also taken into account information for optical spectroscopy. Thus, $[Fe_2(salmp)_2]^{2-}$ shows a weak band at 800 nm with an extinction coefficient ($\epsilon_M = 1010$) compatible with assignment to a d–d transition.[5] Therefore, our solution also required that two of the orbital levels be split by an energy in the range 11 700–13 300 cm^{-1} (850–750 nm).

The solution of Table 3 yields an orbital ground state to which all the t_{2g} wave functions contribute substantially. The listed solution set reflects the situation where the rhombic distortion is small and the axial distortion is approximately along the [111] direction of the cubic frame,[41] implying that the Fe^{2+} environment of $[Fe_2(salmp)_2]^{2-}$ experiences a trigonal rather than tetragonal distortion of the octahedron. This distortion is not evident from an inspection of the crystal structure, which, however, was determined at room temperature.

Table 3. Parameters of $[Fe_2(salmp)_2]^{2-}$ Computed from Ligand-Field Theory

param[a]	computed value
$C_4\langle r^4\rangle$ (cm^{-1})	+55 000
$B_2^{(0)}\langle r^2\rangle$ (cm^{-1})	−1700
$B_2^{(2)}\langle r^2\rangle$ (cm^{-1})	+170
$\angle B_2$ (deg)	30, 55, 30
orbital energies (cm^{-1})	0, 1100, 1700, 11200, 11900
ground orbital wave function	$0.61\|d_{xy}\rangle + 0.46\|d_{xz}\rangle + 0.651\|d_{yz}\rangle$
D_i (cm^{-1}), E_i/D_i[b]	+10, 0.16
$\angle D$ (deg)	50, 52, 61
g_i[b]	2.17, 2.24, 2.00
a_i (MHz)[c]	−13.3, −18.8, −49.8
$\angle a$ (deg)	46, 53, 0
ΔE_Q (mm/s),[d] η	−2.56, +0.4
$\angle$EFG (deg)	42, 56, 56

[a] The quantities $\langle r^n\rangle = \langle t_{2g}|r^n|t_{2g}\rangle$ are expectation values of the radial distribution of the t_{2g} orbitals for a cubic potential. The euler angles $(\alpha\beta\gamma)$[17] rotate the frames of the low-symmetry distortion B_2, $\mathbf{D}_i$-, $\mathbf{a}_i$-, and EFG-tensors relative to the cubic frame. [b] The calculation assumes $\lambda = -100$ cm^{-1}. [c] The calculation assumes $P = 2\beta_e\beta_n g_n/r^3 = 82.3$ MHz[39] and $\kappa = 0.47$[40] for the fermi contact term. [d] The scaling factor in the calculation of the quadrupole interaction is adjusted so that a pure t_{2g} orbital produces $\Delta E_Q = +2.56$ mm/s. In the limit of small spin–orbit interactions, the mixing of the t_{2g} levels will retain the magnitude but not the sign of ΔE_Q.[36]

Conclusion. The study of $[Fe_2(salmp)_2]^{2-}$ has allowed the development of an experimental protocol for the treatment of diferrous clusters in proteins and model systems. The study has provided a stringent test of EPR techniques by showing quantitative predictions at two microwave frequencies and agreement with results from Mössbauer spectroscopy and magnetization measurements. $[Fe_2(salmp)_2]^{2-}$ bears some similarities to the diferrous clusters of proteins; for example, the exchange coupling is ferromagnetic like that observed in MMOH and the azide adducts of RNR and deoxyHr. However, the electronic symmetry of $[Fe_2(salmp)_2]^{2-}$ does not mimic that observed for the proteins, which may be a critical attribute for O_2 activation chemistry of the diferrous clusters of the proteins.

Acknowledgment. We thank Prof. N. Dennis Chasteen (University of New Hampshire) for the use of the Q-band EPR spectrometer and Dr. S.-B. Yu for help in synthesis of the compounds. This work was supported by the Cherry L. Emerson Center for Scientific Computation (Emory University) and the following grants: NIH GM28856 (R.H.H.), NIH GM32394 (E.P.D.), NIH GM49970 (M.P.H.), and NSF DMB9096231 (E.M.).

(37) Champion, P. M. PhD Thesis, University of Illinois, 1975.
(38) The calculations only predict the sign of ΔE_Q. Theoretical attempts at predicting its magnitude for Fe^{2+} complexes have not been successful.
(39) (a) Freeman, A. J.; Watson, R. E. In *Magnetism*; Rado, G. T., Suhl, H., Eds.; Academic Press: New York, 1965; Vol. IIA; p 167. (b) Freeman, A. J.; Watson, R. E. *Phys. Rev.* **1964**, *133*, A1571–A1584. (c) Freeman, A. J.; Watson, R. E. *Phys. Rev.* **1962**, *127*, 2058–2076.
(40) Lang, G.; Marshall, W. *Proc. Phys. Soc.* **1966**, *87*, 3–34.
(41) The Euler angles for an exact rotation to the [111] direction are $\alpha = 45°$, $\beta = 54.7°$, and $\gamma = 0°$.